Weak overturning circulation and high Southern Ocean nutrient utilization maximized glacial ocean carbon

Juan Muglia^{a,*}, Luke C. Skinner^b, Andreas Schmittner^a

^a College of Earth, Ocean and Atmospheric Sciences, Oregon State University, 104 CEOAS
 Administration Building, 101 SW 26th St, Corvallis, OR 97331, USA
 ^b Godwin Laboratory for Palaeoclimate Research, Department of Earth Sciences, Univ. of
 Cambridge, Cambridge CB2 3EQ, UK

Abstract

Circulation changes have been suggested to play an important role in the sequestration of atmospheric CO₂ in the glacial ocean. However, previous studies have resulted in contradictory results regarding the strength of the Atlantic Meridional Overturning Circulation (AMOC) and three-dimensional, quantitative reconstructions of the glacial ocean constrained by multiple proxies remain scarce. Here we simulate the modern and glacial ocean using a coupled physicalbiogeochemical, global, three-dimensional model constrained simultaneously by δ^{13} C, radiocarbon, and δ^{15} N to explore the effects of AMOC differences and Southern Ocean iron fertilization on the distributions of these isotopes and ocean carbon storage. We show that δ^{13} C and radiocarbon data sparsely sampled at the locations of existing glacial sediment cores can be used to reconstruct the modern AMOC accurately. Applying this method to the glacial ocean we find that a surprisingly weak (6-9 Sy or about half of today's) and shallow AMOC maximizes carbon storage and best reproduces the sediment isotope data. Increasing the atmospheric soluble iron flux in the model's Southern Ocean intensifies export production, carbon storage, and further improves agreement with $\delta^{13}\mathrm{C}$ and $\delta^{15}\mathrm{N}$ reconstructions. Our best fitting simulation is a significant improvement compared with previous studies, and suggests that both circulation

Email address: jmuglia@coas.oregonstate.edu (Juan Muglia)

[☆]Fully documented templates are available in the elsarticle package on CTAN.

^{*}Corresponding author

and export production changes were necessary to maximize carbon storage in the glacial ocean.

Keywords: Last Glacial Maximum, Ocean circulation, Carbon cycle

1. Introduction

During the Last Glacial Maximum (LGM, ~ 21 ky before present) atmospheric pCO₂ was about 100 ppm lower than its pre-industrial (PI) value (Marcott et al., 2014). Reconstructions of stable carbon isotope (δ^{13} C) distri-

- butions from LGM sediments indicate a shallower Atlantic Meridional Overturning Circulation (AMOC) and more remineralized nutrients and carbon in the deep Atlantic (Gebbie, 2014). However, no consensus on the glacial AMOC strength exists, with studies inferring weaker (Lynch-Stieglitz et al., 2007), similar (Böhm et al., 2015), or stronger (Kurahashi-Nakamura et al., 2017) overturning rates. Radiocarbon (Δ¹⁴C) reconstructions suggest that the deep ocean
- was more isolated from the atmosphere, which has been suggested to explain the full glacial-interglacial change in atmospheric CO₂ (Sigman et al., 2010; Sarnthein et al., 2013).

On the other hand, an increase in biological production and export of organic matter could have transferred a substantial amount of carbon from the surface and atmosphere to deep waters during the LGM (Martin, 1990). In most of the present Southern Ocean (SO) productivity and macro-nutrient (nitrate, phosphate) utilization is limited by low concentrations of dissolved iron (DFe). Higher dust deposition could have fertilized this region with iron and increased its efficiency as a carbon sink during the LGM. Observations indicate that atmospheric dust fluxes into the SO (Maher et al., 2010; Lambert et al., 2015) and soluble iron content in dust (Conway et al., 2015) were increased in the LGM compared to today, and nutrient utilization (inferred from ¹⁵N/¹⁴N) was more efficient (Martínez-García et al., 2014). However, the effects of increased SO

nutrient utilization and changes in deep ocean circulation on three-dimensional glacial ocean carbon storage remain unquantified.

The goal of this work is to use a model-data comparison to constrain the state of the LGM ocean, including its AMOC, SO nutrient utilization and to separately quantify their effects on ocean carbon storage. We use a three-dimensional, global climate/circulation/biogeochemistry model (Muglia et al., 2017), that includes, for the first time, three key isotopes (14 C, 13 C, 15 N) simultaneously, as well as interactive iron cycling. Previous studies did not use interactive iron cycling (Schmittner & Somes, 2016) or only used individual isotopes (mostly δ^{13} C, Brovkin et al., 2007; Tagliabue et al., 2009; Bouttes et al., 2011; Menviel et al., 2017), which did not allow separation between circulation and export production effects in model/data comparisons. Our comparisons of multiple simulated isotopes with sedimentary reconstructions exploit complementary constraints provided by these isotopes (Schmittner & Somes, 2016)

A detailed analysis of the different components of the ocean's carbon cycle and their effects on atmospheric CO₂ is beyond the scope of this paper and will be presented elsewhere (Khatiwala et al., in preparation).

2. Methods

2.1. Physical and biogeochemical model

and offer novel insights into the glacial ocean.

- We use the global ocean circulation model from the University of Victoria (UVic) (Weaver et al., 2001), version 2.9. It consists of a three-dimensional dynamical ocean with 19 vertical levels at 3.6° × 1.8° horizontal resolution governed by the primitive equations, coupled to a two-dimensional single-level atmosphere, with moisture and heat balances and fluxes between the two mediums, and a dynamical sea ice model. The model is coupled to a dynamic land vegetation model (Meissner et al., 2003). For the pre-industrial simulation wind stress, winds used in air-sea fluxes and horizontal moisture and heat advection, and clouds are prescribed from a present-day monthly climatology (Kalnay et al., 1996). Evaporation, precipitation, air moisture and temperature are calcu-
- by the two-dimensional model. Background vertical diffusivity was set

to 3.5×10^{-5} m²/s. Our diapycnal mixing scheme includes a three-dimensional parametrization of tide effects (Schmittner & Egbert, 2013), but it does not consider changes in tidal energy dissipation. Isopycnal eddy diffusivity was set to 1.2×10^3 m²/s. Higher values are applied in the tropics, to include effects of the Equatorial Intermediate Current System on temperature, salinity and dissolved oxygen (Getzlaff & Dietze, 2013).

LGM runs use an atmospheric CO₂ value of 185 ppm, and orbital parameters corresponding to 21 kyr. Using realistic atmospheric CO₂ is important for an unbiased model-data comparison because fractionation of ¹³C during photosynthesis (Schmittner et al., 2013) and radiocarbon ages (Galbraith et al., 2015) depend on atmospheric CO₂. The wind stress fields include a multi-model mean LGM anomaly from the Paleoclimate Model Intercomparison Project Phase 3 (PMIP3), which are largest over the north Atlantic Ocean due to the presence of the Laurentide Ice Sheet in North America and tend to intensify the AMOC (Muglia & Schmittner, 2015). For the LGM continental ice sheets, we use the reconstruction from the PMIP3 set up (Abe-Ouchi et al., 2015). We also apply a global 1 PSU addition to salinity to account for sea level drop. Changes in river routings were not included. The model's land-sea mask and the resolved bathymetry were not changed from preindustrial conditions.

In LGM runs, the fixed atmospheric CO₂ of 185 ppm forces the ocean to equilibrate its carbon to a lower pre-formed value than in preindustrial runs that use 280 ppm. Thus the global ocean DIC content is lower in LGM than in preindustrial simulations. It is not a goal of this work to infer glacial-interglacial changes in atmospheric CO₂ concentrations, but to compare different modeled LGM configurations with proxy observations, and also to assess their DIC content and distribution. The fact that none of the LGM simulations has a larger DIC inventory than the preindustrial indicates that none of the simulations would result in LGM levels of atmospheric CO₂ in interactive simulations with prognostic atmospheric CO₂ and a constant carbon inventory in the ocean-atmosphere-land system.

UVic is coupled with the Model of Ocean Biogeochemistry and Isotopes

(MOBI), version 1.8. It includes prognostic equations for PO₄, NO₃, DFe, O₂, DIC, dissolved organic matter, particulate organic matter (detritus), particulate iron, phytoplankton, zooplankton and diazotrophs. It is equipped with an advection-diffusion scheme, so tracers depend on ocean physics as well as biogeochemical interactions. The P content of the ocean is assumed constant, but the N cycle includes N₂ fixation by diazotrophs (source of NO₃), and water column and benthic denitrification (sinks of NO₃) (Somes & Oschlies, 2015).

The iron cycle includes external inputs from atmospheric dust deposition, sedimentary release, and hydrothermal fluxes (Muglia et al., 2017). Atmospheric deposition is calculated from a prescribed surface field and added to DFe at the surface. Sedimentary release is proportional to the flux of organic matter reaching the ocean floor, and to a sub-grid bathymetry parameter used to account for unresolved bottom features. Bulk hydrothermal iron fluxes at mid-ocean ridges are added locally to DFe concentrations at the corresponding grid boxes.

2.2. Moisture transport and circulation

Various processes and model parameters can affect the meridional overturning circulation (MOC). Here we modify the meridional southern hemisphere moisture transport (F_{qSH}) , which has been proven to be an efficient way to affect Antarctic Bottom Water (AABW) production and AMOC strength, producing different MOC states. A decreased F_{qSH} leads to saltier AABW and a weaker AMOC (Saenko et al., 2003). It has been suggested that changes in atmospheric water vapor transport played a role in glacial-interglacial changes in SO stratification and CO₂ (Sigman et al., 2007), but estimates of this transport in the LGM are uncertain.

Specific humidity in the UVic model is controlled by the equation

$$\rho_a H \left(\frac{\partial q}{\partial t} + \nabla (\mathbf{u}q) - \nabla (\mu \nabla q) \right) = \rho_o(E - P), \tag{1}$$

where ρ_a and ρ_o are the density of air and water, respectively, H=1.8 km is a scale height, \mathbf{u} is the mean wind velocity for the advection of moisture, E

and P are evaporation and precipitation fluxes, respectively, q is the specific humidity, and μ is the moisture eddy diffusivity. μ accounts for the transport of moisture due to any process that cannot be explained by the resolved advection. It has a trigonometric dependence on latitude (Fig. S1), with higher values at mid latitudes, where eddies play an important role in atmospheric circulation. Larger diffusivities in the southern hemisphere compared with the northern hemisphere improve agreement with modern observations (Saenko et al., 2003), so an anomaly μ_{SH} is added to the moisture diffusivity in the southern hemisphere.

Variations of μ_{SH} produce changes in the meridional transport of humidity from the equator to the SO (Fig. S1), and control the buoyancy of Antarctic Circumpolar waters. Hence we can vary μ_{SH} among experiments and test the effect of different deep circulations and water mass distributions on biogeochemistry, isotopes, radiocarbon ages and carbon storage. We do this by multiplying μ_{SH} by a factor ϵ_q that goes from 1 (default μ_{SH}) to -0.5.

2.3. Iron fluxes

PI and LGM surface soluble iron fluxes were calculated from dust flux monthly climatologies (Lambert et al., 2015, see Muglia et al. (2017) for more details). Compared to the PI, the calculated LGM surface soluble iron fluxes exhibit an increase in parts of the SO, to the east of the Patagonian region and around continents (Fig. S2). Yearly atmospheric surface fluxes to the ocean south of 35° S are 0.009 Tg/y for the PI and 0.018 Tg Fe/y for the LGM. A recent estimation from two Antarctic ice cores suggests that surface soluble iron fluxes into the SO may have been more than 10 times higher during the LGM (Conway et al., 2015). In order to test the effect of an iron fertilization of this kind into the SO, we perform experiments where the LGM atmospheric flux is multiplied by 10 south of 35° S (Fig. S2). In those cases, the yearly atmospheric surface flux to the SO is 0.18 Tg/y.

Sedimentary DFe flux in our model is proportional to the flux of organic carbon reaching the ocean bottom. To calculate it we use a sub-grid bathymetry function that specifies the fraction of ocean bottom at each ocean grid box, and is multiplied to the sedimentary release (Muglia et al., 2017). Lower sea level in the LGM exposed a fraction of present day continental shelves, so for LGM runs we lowered sea level by 125 m (Lambeck et al., 2014) in the topography map used to calculate the sub-grid bathymetry. This results in lower sedimentary fluxes around continents (Fig. S2).

150 2.4. Experiments

Table 1 lists all LGM experiments that include biogeochemistry and isotopes. Each was run for 5 ky, and results from the last 500 years are shown. Experiments differ in their ocean circulation (obtained by varying F_{qSH} , see 2.2) and in additional SO soluble iron fluxes (see 2.3). Experiment labels are defined by their AMOC strength at 25° N. The SOFe label indicates models where the LGM atmospheric soluble iron flux was multiplied by 10 between 35° S and Antarctica. Stable isotope and radiocarbon data used to compare our simulations to, as well as the comparison methods we use, are described in the Supplementary Materials (SM).

2.5. Validation

In order to test our methodology, we seek to answer the following question: Can the modern AMOC be reconstructed by fitting the model to observed δ^{13} C and radiocarbon ages sub-sampled on the relatively sparse sediment core locations available for the LGM ocean? For this test, we have produced different PI simulations with AMOC's ranging between 11.5 and 18.4 Sv. Root mean square errors (RMSE) range between $180-290^{-14}$ Cyr in radiocarbon and 0.28-0.36% in δ^{13} C (Fig. 1). The best fit, considering both correlation coefficient R and RMSE as metrics, to both top-core δ^{13} C and natural radiocarbon age, sampling only where LGM observations are available, is a simulation with AMOC strength of 17.8 Sv. This is consistent with independent estimates (17.2 \pm 0.9 Sv, McCarthy et al., 2015) from modern observations (Fig. 1). The result indicates that δ^{13} C and radiocarbon reconstructions given at the relatively sparse sampling of the LGM can be used to quantitatively reconstruct the AMOC.

3. Results

3.1. Physics and biogeochemistry

The model's LGM AMOC decreases continuously with decreasing F_{qSH} until about 6 Sv (Fig. 2; Table S1), at which point the AMOC collapses. It exhibits hysteresis behavior that is impacted by North Atlantic wind stress changes by decreasing the width of the hysteresis curve and shifting it towards lower F_{qSH} values (Fig. 2, bottom left). AMOC states between 0 and 6 Sv are unstable.

The stronger wind stress over the North Atlantic that existed during the LGM as a consequence of the Laurentide Ice Sheet (Ullman et al., 2014; Muglia & Schmittner, 2015), considered in our prescribed wind stress fields, stabilizes the weak LGM AMOC by increasing the gyre circulation and maintaining relatively high salinities in the North Atlantic (Fig. 2). It also produces the conspicuous deepening of the North Atlantic Deep Water (NADW) in LGM_13.

Preindustrial minimum and maximum SO sea ice surfaces in PI_control are 1.6 and 19.9 × 10⁶ km², respectively. This represents an underestimation of summer sea ice extension with respect to observations of 4.12 ± 0.8 × 10⁶ km², although winter extension is well captured compared to 21 ± 2 × 10⁶ km² in Roche et al. (2012). Conversely, all our LGM simulations, which range from 7 (LGM_13) to 13 × 10⁶ km² (LGM_6), are in good agreement with LGM minimum sea extent reconstructions (11.1 ± 4 × 10⁶ km², Roche et al., 2012), but underestimate LGM maximum sea ice extent (from 30 (LGM_13) to 35 (LGM_6) × 10⁶ km² versus 43.5 ± 4 × 10⁶ km² in Roche et al., 2012). This indicates that the LGM-PI difference in SO sea ice extent seasonal amplitude is underestimated in our simulations.

LGM-PI_control mean surface air temperature anomalies range between -4.6 and -4.9 °C, in agreement with observations (Annan & Hargreaves, 2013). Global mean ocean temperature anomalies range between -1.8 °C in LGM_13 to -2.4 °C in LGM_8 and LGM_6, with the latter being the value closest to a recent reconstruction of -2.57 ± 0.24 °C (Bereiter et al., 2018).

LGM-PI_control sea surface temperature (SST) anomalies are in the range

of reconstructions from MARGO (Waelbroeck et al., 2009) for the Atlantic (Fig. 2) and Indo-Pacific (Fig. S3) oceans, with some cold biases, especially at northern high latitudes. MARGO's predicted cooling of -2 °C is overestimated by our simulations, which range between -2.5 to -2.6 °C. Statistically, all LGM experiments are in similarly good agreement with MARGO, with a range of correlation coefficient (R) of 0.93-0.95 and root mean square error (RMSE) of 2.8-3.0 °C, which shows the skill of our model to reproduce LGM SST's, but at the same time illustrates the inability of SST data to constrain the LGM AMOC.

LGM meridional moisture fluxes cannot be easily constrained by data, so our prescribed fluxes are not validated by observations. However, at mid-latitudes the difference between the moisture transport of the weak AMOC cases and the modern observations is similar to the difference between the modern reanalysis data and PI_control (Fig. S1). Given those uncertainties, the applied fluxes in the model are not unreasonable.

Lower meridional moisture fluxes decrease precipitation south of 45° S. As a result, surface salinities increase around Antarctica and decrease in sub-polar regions in experiments with decreased F_{qSH} relative to LGM_13 (Fig. S4). The surface SO cools, buoyancy loss and sea ice extent increase around Antarctica, and Antarctic Bottom Water (AABW) production is enhanced, as hypothesized by (Ferrari et al., 2014). In LGM_8 e.g., AABW reaches far into the deep North Atlantic (NA), and the interface with NADW becomes 700 – 1000 m shallower (Fig. 2). The AMOC is weak and shallow compared to LGM_13 and PI control.

Circumpolar deep water inflow into the Indian and Pacific oceans and the associated MOC (IPMOC) is also weakened due to reduced NADW inflow into the Southern Ocean (Fig. S3, Table 1). Higher meridional pressure gradients increase Antarctic Circumpolar Current transport in LGM_8 compared to LGM_13 and PI_control (Table S1), consistent with δ^{18} O reconstructions (Lynch-Stieglitz et al., 2016).

AABW is saltier than NADW in LGM 8 (Fig. 2), in agreement with sed-

imentary pore-water reconstructions (Adkins et al., 2002; Insua et al., 2014).

LGM_13 has salinity distributions more similar to PI_control, but since porewater reconstructions remain relatively sparse and have high uncertainties (Miller et al.,
2015; Wunsch, 2016), salinity fields alone are insufficient to rule it out as a possible LGM scenario.

Lower surface temperatures and increased sea ice cover decrease primary 240 productivity and export production from PI control to LGM runs in the SO (Fig. 3) due to enhanced light limitation of phytoplankton. This is exacerbated in the weak AMOC cases, mainly because of their increased sea ice cover around Antarctica. In accordance, surface nutrients are increased in this region in LGM experiments (Fig. S5). LGM iron fluxes from Lambert et al. (2015) do not produce a considerable effect on biogeochemistry compared to PI control (Muglia et al., 2017), similar to what the authors of that work found when they applied the same fluxes (assuming constant solubility) to an ocean model. On the other hand, SOFe experiments (see 2.4) do show an increase in SO productivity and export production, northward of the position of summer sea ice. In Fig. 3, the region of increased export production reaches further south for LGM 13 SOFe because of less grid boxes being occupied by sea ice in this experiment compared to LGM_8_SOFe. The latter experiment is in better agreement with reconstructions of LGM-PI export production changes from a variety of proxies, which suggest increased (reduced) production north (south) of the Polar Front (Kohfeld et al., 2013, and K. Kohfeld, personal communication). Surface nutrients decrease in the region of higher productivity, but increase south of that (Fig. S5), and a high nutrient signal is transferred between AABW and deep waters (not shown). A future work will focus on the decomposition of nutrients and carbon in these experiments.

3.2. Radiocarbon

Please see the SM for a description of our radiocarbon model. Our LGM experiments predict older (in ¹⁴Cyr) waters than PI_control in most of the deep ocean (Fig. 4). Even LGM_13, which has a similar although slightly reduced

MOC compared to PI control, results in $\sim 300^{-14}$ Cyr older radiocarbon ages (Table S2) due to increased sea ice cover and lower pCO₂ (Galbraith et al., 2015). However, old LGM radiocarbon ages in the deep NA and Pacific predicted by reconstructions (Skinner et al., 2017) are only reproduced with a weak (or collapsed) AMOC and increased AABW. In the Atlantic, LGM 8 exhibits a clear separation between AABW with ages higher than 2000 ¹⁴Cyr and NADW with ages younger than 1000 ¹⁴Cyr at approximately 2500 m of water depth. Compared to PI control, the depth of the interface shoals by about 1000 m and vertical gradients are much enhanced. Experiments LGM_9, LGM_8 and LGM 6 fit the sediment data best, as indicated by their higher R and lower uncertainty-normalized RMSE (Fig. 4, Table S2). The difference in absolute (unnormalized) RMSE between these experiments and the worse fitting ones is of the order of 100 ¹⁴Cyr, similar to the difference among preindustrial goodand bad-fitting runs (Fig. 1). The best fitting simulations' RMSE's of ~ 1.1 indicate that these experiments are consistent with the observations given the error estimates. RMSE's of ~ 1.3 for LGM_0 and LGM_13 indicate that 280 these simulations have 20 % larger errors and thus are considerably less consistent with the observations. This provides significant evidence that the LGM AMOC was active, but likely weaker than in modern times. A comparison of PI control radiocarbon ages with LGM observations gives normalized RMSE of 1.5, considerably higher than all LGM simulations. This suggests that our preindustrial circulation does a worse job than any of our LGM states at reproducing deep LGM ¹⁴C ages, in apparent conflict with a recent box model study that suggests that a modern circulation can reproduce them (Zhao et al., 2018).

Reconstructions of LGM radiocarbon ages from sediment cores are much noisier than modern water column measurements, indicating errors or biases in the reconstructions. Reconstructions (Skinner et al., 2017) mapped to our model's grid suggest a global LGM-PI difference of 673 – 936Cyr. The global age differences between our LGM experiments and PI_control, calculated over grid boxes for which LGM data exist, vary between 283 and 635 ¹⁴Cyr (Fig. 4, Table S2), with LGM 6 producing the highest estimate. If we consider all model

grid boxes, LGM_6 produces a maximum aging of 635 14 Cyr, close to a global interpolated estimate of 689 ± 53 14 Cyr (Skinner et al., 2017). At depths below 2000 m, the simulations result in 281 to 828 14 Cyr older waters, and LGM_9 is closest to sedimentary reconstructions of 600 14 Cyr (Sarnthein et al., 2013; Skinner et al., 2017).

Discrepancies between our model and reconstructions could be related to high variability in the reconstructed surface reservoir ages, which were calculated either as modern reservoir ages plus 250 $^{14}\mathrm{Cyr}$ (due to pCO₂ effects, Galbraith et al., 2015) or from independent dating. They have a global mean LGM-PI value of 285 $^{14}\mathrm{Cyr}$ and higher LGM variability (388 $^{14}\mathrm{Cyr}$) than our modeled estimates (Fig. S6), which exhibit an LGM-PI_control range of 247 to 255 $^{14}\mathrm{Cyr}$ and have an LGM variability of $\sim 130~^{14}\mathrm{Cyr}$. Using surface reservoir ages from LGM_6 to re-calculate LGM radiocarbon ages from observed benthic-planktonic age differences (Skinner et al., 2017) gives a mean LGM-PI aging of 673 $^{14}\mathrm{Cyr}$ (lower orange dashed line in Fig. 4). Our highest estimate of 635 $^{14}\mathrm{Cyr}$ is close to this number, indicating that surface reservoir ages are a significant cause of difference between modeled and reconstructed ventilation ages.

3.3. Stable isotopes

A strong presence of high δ¹³C NADW in the Atlantic as exhibited by LGM_13 is inconsistent with LGM reconstructions (Fig. 5). This simulation also produces too high Pacific δ¹³C, especially in the southern hemisphere. In LGM_8 low δ¹³C AABW penetrates into the northern hemisphere (NH), and high δ¹³C waters are confined to the upper 1500 m of the NA, consistent with observations (Peterson et al., 2014). A vertical profile of global δ¹³C means from LGM_8 reproduces the decrease in reconstructed δ¹³C with depth, in contrast to LGM_13, which results in a mid-depth maximum, and LGM_0, which results in a mid-depth minimum (Fig. 5, bottom right). LGM_8 is in better agreement with observations than the strong and collapsed AMOC cases (Table S2).

Higher SO atmospheric soluble iron flux in SOFe experiments increases phytoplankton productivity, carbon export, and deep DIC (Muglia et al., 2017), intensifying δ^{13} C depletion in the AABW of the Atlantic sector (LGM_13_SOFe and LGM_8_SOFe in Fig. 5). It also produces too low δ^{13} C in the deep Pacific compared to observations, probably because most of the LGM's extra dust originated in Patagonia and delivered to the south Atlantic primarily (Lambert et al., 2015), so fluxes over the south Pacific may be overestimated in our SOFe experiments.

330

The representation of δ¹³C compared to observations improves in all LGM
cases when higher atmospheric iron fluxes are applied (Fig. 5, bottom). LGM_8_SOFe
exhibits the highest R (0.79) and lowest uncertainty-normalized RMSE (1.20,
Table S2). The unnormalized RMSE is 0.33 ‰, of the same order of magnitude
as the combined model-data uncertainty (0.28 ‰). This value indicates that this
experiment's error is only 20 % larger than that of the PI_control simulation
relative to the late Holocene core-top data. RMSE for the collapsed and strong
AMOC cases is more than double, which indicates that those simulations are
inconsistent with the observations.

SOFe experiments produce higher nutrient utilization and organic matter $\delta^{15}N$ in the SO, improving considerably the agreement with LGM-PI reconstructions (Fig. 6). The model/observation R is more than 50% higher in these experiments than in the rest (Table S2). Part of the extra iron is transported and upwelled to the eastern equatorial Pacific, increasing that region's primary productivity, nitrate utilization and water column denitrification (Fig. S5), in agreement with some observations from sediment cores (Winckler et al., 2016), although other observations suggest that higher iron in the SO should cause lower productivity in the equatorial Pacific because of higher consumption of other nutrients (Costa et al., 2016). In our model the effect increases $\delta^{15}N$ locally, giving a better agreement with observed LGM-PI changes.

Circulation changes have a smaller effect on $\delta^{15}N$ than iron fertilization (Fig. 6). Among the SOFe experiments, the ones with weaker circulation provide a slightly better fit to the data, due to a better estimation of SO $\delta^{15}N$ increase

and the reproduction of positive $\delta^{15}N$ anomalies in the tropical Atlantic.

4. Discussion

Our experiments indicate that a remarkably weak, shallow AMOC with increased AABW entrainment to the Atlantic Ocean is consistent with LGM reconstructions of radiocarbon age and δ^{13} C. This suggests that LGM AMOC strength at 25° N may have been between 6 and 9 Sv (Table 1), with a NADW shallowing of 1000-1500 m with respect to PI, and that NADW export into the SO was decreased by about two thirds from 15 Sv in PI to 5 Sv in LGM_8 (Fig. 2). They indicate a weaker AMOC than suggested by previous studies (Brovkin et al., 2007; Bouttes et al., 2011; Menviel et al., 2017) but qualitatively consistent with interpretations of LGM proxy data (Lynch-Stieglitz et al., 2007). Since the AMOC in our model is not stable for values lower than 6 Sv, we cannot evaluate even weaker but non-collapsed states. Nevertheless, the poor agreement between a collapsed state and reconstructions rules out that possibility.

A recent data assimilation study (Kurahashi-Nakamura et al., 2017) inferred a shallow and strong LGM AMOC (22 Sv), which resulted in a global LGM δ^{13} C RMSE of 0.50 ‰. This is in qualitative agreement with interpretations of 231 Pa/ 230 Th and neodymium data from the Atlantic Ocean (Lippold et al., 2016). Our best estimate (LGM_8_SOFe) exhibits an RMSE of 0.33 ‰ to the same δ^{13} C data used in Kurahashi-Nakamura et al. (2017), considerably lower than their error. Note that RMSE of ~ 0.3 ‰ is typical for our best fitting PI simulations (Fig. 1). On the other hand, a RMSE of 0.5 ‰ is much larger than any of the PI simulations examined here and 50 % larger than our best fitting LGM simulation. This indicates that the strong and shallow AMOC model of Kurahashi-Nakamura et al. (2017) does not fit the LGM δ^{13} C observations well, in contrast with our shallow and weak simulations, which fit the reconstructions much better. Our results (Fig. 4) suggest that a stronger LGM AMOC would have caused too low LGM-PI radiocarbon age differences compared to recon-

structions (Skinner et al., 2017), although a previous, more restricted data set of radiocarbon from the Brazil margin indicates that the LGM ventilation was not very different from the modern in that region (Freeman et al., 2016). We conclude that a shallow and strong AMOC is less in agreement with the whole range of existing δ^{13} C and radiocarbon observations than a shallow and weak AMOC, but that scenario may not be discarded given that it has not been tested in our model simulations.

Another recent study (Menviel et al., 2017) found the best match to LGM-PI $\Delta \delta^{13}$ C to be a simulation with stronger AMOC than our LGM estimates and weaker global AABW transport $(10 - 15 \text{ and } \le 10 \text{ Sy}, \text{ respectively, in})$ Menviel et al. (2017) versus 8 and 17 Sv in LGM 8 and LGM 8 SOFe, Table S1). This represents a possible alternative circulation configuration that we have not assessed in our experiments, as AABW transport in our best estimates is of similar magnitude than its PI control value instead of weaker. However, LGM 8 SOFe produces a slightly better fit to the same $\Delta \delta^{13}$ C reconstruction (R=0.63 and RMSE=0.31 % in LGM 8 SOFe versus 0.6 and 0.33 %in Menviel et al. (2017)), while also including iron fertilization effects, and the additional constraint from $\delta^{15}N$ and radiocarbon. Our estimate also agrees well with $\delta^{18}{\rm O}$ evidence of increased Antarctic Circumpolar Current transport in the LGM (Lynch-Stieglitz et al., 2016, Table S1), something that was not tested by Menviel et al. (2017). We conclude that both works agree in the existence of a weaker and shallower AMOC during the LGM, but it is debatable whether AABW circulation was of similar magnitude or weaker. This remains an important question to address in the future.

A tenfold increase in SO atmospheric soluble iron flux, as suggested by ice core data (Conway et al., 2015), increases distribution of LGM δ^{13} C and LGM-PI δ^{15} N compared to observations. In the SO of LGM_8_SOFe, LGM-PI export production changes are positive in a band between 45° S and 60° S, and are negative south of that (Fig. 3), qualitatively similar to estimates from a variety of proxies (Kohfeld et al., 2013).

410

We tested iron fertilizations higher than the 10×LGM experiment presented

here, finding little additional effect on the biogoechemistry and δ^{15} N, and a worse fit to δ^{13} C observations (Fig. 7, circles). Scavenging acts to remove the extra DFe in these cases, preventing a higher increase in nutrient uptake by phytoplankton, indicating a saturation effect. A more realistic iron cycle that includes interactive ligands (Völker & Tagliabue, 2015) and/or phytoplankton species shifts (Moore et al., 2000) could potentially further improve the agreement with δ^{15} N reconstructions.

An additional simulation generated with a tenfold increase in LGM atmospheric soluble iron deposition over the whole ocean, instead of just the SO, produces a 50 % lower R, indicating that the enhanced export production must have been restricted to the SO (Fig. S7). This global iron-fertilization simulation overestimates LGM-PI δ^{15} N changes in the SO and elsewhere due to too much suboxia, water-column denitrification and nitrogen fixation, similar to experiments with globally increased phytoplankton growth rates (Schmittner & Somes, 2016).

In conclusion, our simulations suggest that in order to reproduce the combination of reconstructed LGM radiocarbon ages, $\delta^{13}\mathrm{C}$ of DIC and $\delta^{15}\mathrm{N}$ of organic matter, a weak, shallow NADW and a voluminous AABW, together with increased export production in the SO, are needed. To our knowledge, this is the first time that these three properties are generated by a coupled physical-biogeochemical global ocean model that includes a prognostic iron cycle, and are directly compared to LGM reconstructions. The estimated AMOC strength at 25° N is 6-9 Sv and the IPMOC at 30° S is 12-13 Sv $(-50\,\%$ and $-20\,\%$ change, respectively). Note that our experimental design explores only a limited parameter space. For this reason we cannot exclude that other circulations and/or biogeochemical forcings fit the data similarly well or better. However, our solutions represent a baseline that can be improved upon in the future.

What impacts did such a state have on the carbon storage of the glacial ocean? Global mean LGM-PI ΔDIC are negative in our simulations (Table 1), because of the fixed 185 ppm atmospheric CO₂ applied to our ocean model, which forces it to equilibrate at lower carbon concentrations, and the absence

of changes in global alkalinity (Schmittner & Somes, 2016). However, a weak AMOC and far-reaching AABW produce higher accumulation of dissolved inorganic carbon (DIC) than a collapsed or strong circulation (Fig. 7, Table 1), presumably maximizing during glacial states the amount of respired and/or disequilibrium deep ocean carbon (Skinner, 2009).

Compared to the strong circulation LGM case, a weak and shallow AMOC state (e.g., LGM 8) increases carbon accumulation in deep and bottom waters in both the Atlantic and Indo-Pacific oceans (Fig. 8), due to a higher volume of poorly-ventilated, SO-originated, high-DIC waters occupying these regions. Remineralized nutrients approximated using Apparent Oxygen Utilization (AOU) increase in the deep ocean (Fig. S8), particularly in the North Atlantic where NADW is replaced by AABW. Preformed nutrients (Fig. S9) are reduced everywhere except in the less ventilated parts of the Atlantic Ocean. This contrasts with results from a reduced circulation experiment from North Atlantic Ocean hosing (Schmittner & Galbraith, 2008), where preformed nutrient presence increased in most of the deep ocean. However, in that experiment the hosing of the North Atlantic produced an increase in SST and a decrease in sea ice in the SO, opposite to the effect of our southern hemisphere-driven forcing (Fig. S4). Thus, in our weak and shallow AMOC experiments, increased SO sea ice decreases export production and preformed nutrients are reduced. The effect is partly countered in the collapsed AMOC case LGM 0 (not shown), which exhibits less SO sea ice and higher SST than the weak AMOC cases, and thus has a slightly lowered DIC content than the latter. A detailed and accurate carbon decomposition as well as effects on atmospheric CO₂ will be presented elsewhere (Khatiwala et al., in preparation). It is expected that the impact on atmospheric CO₂ will depend crucially on how the effects of export production, circulation, sea ice and solubility interact to influence both the respired and the disequilibrium carbon inventories of the global ocean (Skinner, 2009; Ito & Follows, 2013).

Increasing export production through SO iron fertilization also raises DIC (Fig. 7), due to a higher efficiency of the biological pump in the SO. The

DIC increase is larger than that from circulation changes, similar to previous works (Brovkin et al., 2007; Tagliabue et al., 2009), although the two effects are likely to interact in a non-linear manner. AABW disseminates the extra carbon in the deep ocean (Fig. 8), so LGM_8_SOFe and LGM_6_SOFe, where this water mass is most voluminous, exhibit the highest ocean carbon content. The combination of circulation and iron fertilization effects provides evidence against suggestions that either iron fertilization (e.g. Martínez-García et al., 2014) or circulation (e.g. Sarnthein et al., 2013) effects alone can explain the whole glacial-interglacial change in ocean carbon content.

5. Conclusion

A weak but stable AMOC and high SO export production together produce higher global ocean carbon than other LGM ocean configurations. This configuration is also the one that best reproduces carbon and nitrogen isotope fields. This suggests that a weak and shallow AMOC together with increased SO export production provide a viable state of the LGM ocean. Those features may also provide important mechanisms for atmospheric CO₂ trapping in the deep ocean during glacial periods. These constitute baseline states that can be compared in the future with other solutions to further refine our understanding of the glacial ocean.

6. Acknowledgements

Study supported by NSF's Marine Geology and Geophysics program (OCE1131834, OCE-1235544). LCS acknowledges funding from NERC grant NE/L006421/1.
The IPODS project provided JM with funding to present results in the 2nd IPODS Workshop.

7. Data availability

Model results can be found in the NOAA's paleoclimate repository (https://www.ncdc.noaa.gov/paleosos search/study/22431).

References

510

- Abe-Ouchi, A., Saito, F., Kageyama, M., Braconnot, P., Harrison, S., Lambeck, K., Otto-Bliesner, B., Peltier, W., Tarasov, L., Peterschmitt, J.-Y. et al. (2015). Ice-sheet configuration in the CMIP5/PMIP3 Last Glacial Maximum experiments. Geoscientific Model Development, 8.
- Adkins, J. F., McIntyre, K., & Schrag, D. P. (2002). The salinity, temperature, and $\delta 180$ of the glacial deep ocean. *Science*, 298, 1769–1773.
- Annan, J., & Hargreaves, J. (2013). A new global reconstruction of temperature changes at the Last Glacial Maximum. Climate of the Past, 9, 367.
- Bereiter, B., Shackleton, S., Baggenstos, D., Kawamura, K., & Severinghaus, J. (2018). Mean global ocean temperatures during the last glacial transition. Nature, 553, 39.
 - Böhm, E., Lippold, J., Gutjahr, M., Frank, M., Blaser, P., Antz, B., Fohlmeister, J., Frank, N., Andersen, M., & Deininger, M. (2015). Strong and deep Atlantic meridional overturning circulation during the last glacial cycle. *Nature*, 517, 73–76.
 - Bouttes, N., Paillard, D., Roche, D. M., Brovkin, V., & Bopp, L. (2011). Last Glacial Maximum CO2 and $\delta 13$ C successfully reconciled. Geophysical Research Letters, 38.
- Brovkin, V., Ganopolski, A., Archer, D., & Rahmstorf, S. (2007). Lowering of glacial atmospheric CO2 in response to changes in oceanic circulation and marine biogeochemistry. *Paleoceanography*, 22.
- Conway, T. M., Wolff, E. W., Röthlisberger, R., Mulvaney, R., & Elderfield, H. (2015). Constraints on soluble aerosol iron flux to the Southern Ocean at the Last Glacial Maximum. *Nature communications*, 6, 7850.
 - Costa, K., McManus, J., Anderson, R., Ren, H., Sigman, D., Winckler, G., Fleisher, M., Marcantonio, F., & Ravelo, A. (2016). No iron fertilization in the equatorial Pacific ocean during the last ice age. *Nature*, 529, 519–522.

- Ferrari, R., Jansen, M. F., Adkins, J. F., Burke, A., Stewart, A. L., & Thompson, A. F. (2014). Antarctic sea ice control on ocean circulation in present and glacial climates. *Proceedings of the National Academy of Sciences*, 111, 8753–8758.
 - Freeman, E., Skinner, L. C., Waelbroeck, C., & Hodell, D. (2016). Radiocarbon evidence for enhanced respired carbon storage in the atlantic at the last glacial maximum. *Nature communications*, 7, 11998.

- Galbraith, E. D., Kwon, E. Y., Bianchi, D., Hain, M. P., & Sarmiento, J. L. (2015). The impact of atmospheric pCO2 on carbon isotope ratios of the atmosphere and ocean. Global Biogeochemical Cycles, 29, 307–324.
- Gebbie, G. (2014). How much did Glacial North Atlantic Water shoal? *Paleo-*ceanography, 29, 190–209.
 - Getzlaff, J., & Dietze, H. (2013). Effects of increased isopycnal diffusivity mimicking the unresolved equatorial intermediate current system in an earth system climate model. *Geophysical Research Letters*, 40, 2166–2170.
- Insua, T. L., Spivack, A. J., Graham, D., D'Hondt, S., & Moran, K. (2014).
 Reconstruction of Pacific Ocean bottom water salinity during the Last Glacial Maximum. Geophysical Research Letters, 41, 2914–2920.
 - Ito, T., & Follows, M. J. (2013). Air-sea disequilibrium of carbon dioxide enhances the biological carbon sequestration in the southern ocean. Global Biogeochemical Cycles, 27, 1129–1138.
- Kalnay, E., Kanamitsu, M., Kistler, R., Collins, W., Deaven, D., Gandin, L., Iredell, M., Saha, S., White, G., Woollen, J. et al. (1996). The NCEP/NCAR reanalysis 40-year project. Bulletin of the American Meteorological Society, 77, 437–471.
- Key, R. M., Kozyr, A., Sabine, C. L., Lee, K., Wanninkhof, R., Bullister, J. L.,
 Feely, R. A., Millero, F. J., Mordy, C., & Peng, T.-H. (2004). A global ocean

- carbon climatology: Results from Global Data Analysis Project (GLODAP). Global Biogeochemical Cycles, 18.
- Kohfeld, K., Graham, R., De Boer, A., Sime, L., Wolff, E., Le Quéré, C., & Bopp, L. (2013). Southern hemisphere westerly wind changes during the Last Glacial Maximum: paleo-data synthesis. *Quaternary Science Reviews*, 68, 76–95.

575

- Kurahashi-Nakamura, T., Paul, A., & Losch, M. (2017). Dynamical reconstruction of the global ocean state during the Last Glacial Maximum. *Paleoceanography*, 32, 326–350.
- Lambeck, K., Rouby, H., Purcell, A., Sun, Y., & Sambridge, M. (2014). Sea level and global ice volumes from the Last Glacial Maximum to the Holocene.
 Proceedings of the National Academy of Sciences, 111, 15296–15303.
 - Lambert, F., Tagliabue, A., Shaffer, G., Lamy, F., Winckler, G., Farias, L., Gallardo, L., Pol-Holz, D. et al. (2015). Dust fluxes and iron fertilization in Holocene and Last Glacial Maximum climates. *Geophysical Research Letters*, 42, 6014–6023.
 - Lippold, J., Gutjahr, M., Blaser, P., Christner, E., de Carvalho Ferreira, M. L., Mulitza, S., Christl, M., Wombacher, F., Böhm, E., Antz, B. et al. (2016). Deep water provenance and dynamics of the (de) glacial Atlantic meridional overturning circulation. *Earth and planetary science letters*, 445, 68–78.
 - Lynch-Stieglitz, J., Adkins, J. F., Curry, W. B., Dokken, T., Hall, I. R., Herguera, J. C., Hirschi, J. J.-M., Ivanova, E. V., Kissel, C., Marchal, O. et al. (2007). Atlantic meridional overturning circulation during the Last Glacial Maximum. Science, 316, 66–69.
- Lynch-Stieglitz, J., Ito, T., & Michel, E. (2016). Antarctic density stratification and the strength of the circumpolar current during the Last Glacial Maximum. Paleoceanography, 31, 539–552.

- Maher, B., Prospero, J., Mackie, D., Gaiero, D., Hesse, P., & Balkanski, Y. (2010). Global connections between aeolian dust, climate and ocean biogeochemistry at the present day and at the Last Glacial Maximum. *Earth-Science Reviews*, 99, 61–97.
 - Marcott, S. A., Bauska, T. K., Buizert, C., Steig, E. J., Rosen, J. L., Cuffey, K. M., Fudge, T., Severinghaus, J. P., Ahn, J., Kalk, M. L., McConnell, J. R., Sowers, T., Taylor, K. C., White, J. W. C., & J, B. E. (2014). Centennial-scale changes in the global carbon cycle during the last deglaciation. *Nature*, 514, 616-619.

- Martin, J. H. (1990). Glacial-interglacial CO2 change: The iron hypothesis. Paleoceanography, 5, 1–13.
- Martínez-García, A., Sigman, D. M., Ren, H., Anderson, R. F., Straub, M.,
 Hodell, D. A., Jaccard, S. L., Eglinton, T. I., & Haug, G. H. (2014). Iron fertilization of the Subantarctic Ocean during the last ice age. Science, 343, 1347–1350.
- McCarthy, G., Smeed, D., Johns, W., Frajka-Williams, E., Moat, B., Rayner,
 D., Baringer, M., Meinen, C., Collins, J., & Bryden, H. (2015). Measuring
 the Atlantic meridional overturning circulation at 26 N. Progress in Oceanography, 130, 91–111.
 - Meissner, K., Weaver, A., Matthews, H., & Cox, P. (2003). The role of land surface dynamics in glacial inception: a study with the Uvic Earth System Model. *Climate Dynamics*, 21, 515–537.
- Menviel, L., Yu, J., Joos, F., Mouchet, A., Meissner, K., & England, M. (2017).

 Poorly ventilated deep ocean at the Last Glacial Maximum inferred from carbon isotopes:a data-model comparison study. *Paleoceanography*, 32, 2–17.
 - Miller, M. D., Simons, M., Adkins, J. F., & Minson, S. E. (2015). The information content of pore fluid δ18O and [Cl-]. *Journal of Physical Oceanography*, 45, 2070–2094.

- Moore, J. K., Abbott, M. R., Richman, J. G., & Nelson, D. M. (2000). The Southern Ocean at the Last Glacial Maximum: A strong sink for atmospheric carbon dioxide. *Global Biogeochemical Cycles*, 14, 455–475.
- Muglia, J., & Schmittner, A. (2015). Glacial Atlantic overturning increased by wind stress in climate models. *Geophysical Research Letters*, 42, 9862–9868.
 - Muglia, J., Somes, C. J., Nickelsen, L., & Schmittner, A. (2017). Combined effects of atmospheric and seafloor iron fluxes to the glacial ocean. *Paleo-ceanography*, 32, 1204–1218.
- Peterson, C. D., Lisiecki, L. E., & Stern, J. V. (2014). Deglacial whole-ocean δ 13C change estimated from 480 benthic foraminiferal records. *Paleoceanog-raphy*, 29, 549–563.
 - Roche, D., Crosta, X., & Renssen, H. (2012). Evaluating Southern Ocean sea-ice for the Last Glacial Maximum and pre-industrial climates: PMIP-2 models and data evidence. *Quaternary Science Reviews*, 56, 99–106.
- Saenko, O. A., Weaver, A. J., & Schmittner, A. (2003). Atlantic deep circulation controlled by freshening in the Southern Ocean. Geophysical Research Letters, 30.
 - Sarnthein, M., Schneider, B., & Grootes, P. M. (2013). Peak glacial 14C ventilation ages suggest major draw-down of carbon into the abyssal ocean. *Climate of the Past*, 9, 2595–2614.

- Schmittner, A., Bostock, H. C., Cartapanis, O., Curry, W. B., Filipsson, H. L., Galbraith, E. D., Gottschalk, J., Herguera, J. C., Hoogakker, B., Jaccard, S. et al. (2017). Calibration of the carbon isotope composition (δ13C) of benthic foraminifera. *Paleoceanography*, 32, 512–530.
- Schmittner, A., & Egbert, G. (2013). An improved parameterization of tidal mixing for ocean models. Geoscientific Model Development, 6, 4475–4509.

- Schmittner, A., & Galbraith, E. D. (2008). Glacial greenhouse-gas fluctuations controlled by ocean circulation changes. *Nature*, 456, 373–376.
- Schmittner, A., Gruber, N., Mix, A., Key, R., Tagliabue, A., & Westberry,
 T. (2013). Biology and air–sea gas exchange controls on the distribution of carbon isotope ratios (δ 13 c) in the ocean. Biogeosciences, 10, 5793–5816.
 - Schmittner, A., & Somes, C. J. (2016). Complementary constraints from carbon (13C) and nitrogen (15N) isotopes on the glacial ocean's soft-tissue biological pump. *Paleoceanography*, 31, 669–693.
- Sigman, D. M., De Boer, A. M., & Haug, G. H. (2007). Antarctic stratification, atmospheric water vapor, and heinrich events: A hypothesis for late Pleistocene deglaciations. Ocean Circulation: Mechanisms and Impacts-Past and Future Changes of Meridianal Overturning, (pp. 335–349).
- Sigman, D. M., Hain, M. P., & Haug, G. H. (2010). The polar ocean and glacial cycles in atmospheric CO2 concentration. *Nature*, 466, 47–55.
 - Skinner, L. (2009). Glacial-interglacial atmospheric CO2 change: a possible "standing volume" effect on deep-ocean carbon sequestration. Climate of the Past, 5, 537–550.
- Skinner, L., Primeau, F., Freeman, E., de la Fuente, M., Goodwin, P.,
 Gottschalk, J., Huang, E., McCave, I., Noble, T., & Scrivner, A. (2017).
 Radiocarbon constraints on the glacial ocean circulation and its impact on atmospheric CO2. Nature Communications, 8.
 - Somes, C. J., & Oschlies, A. (2015). On the influence of âÅIJnon-RedfieldâÅİ dissolved organic nutrient dynamics on the spatial distribution of N2 fixation and the size of the marine fixed nitrogen inventory. Global Biogeochemical Cycles, 29, 973–993.

Tagliabue, A., Bopp, L., Roche, D., Bouttes, N., Dutay, J.-C., Alkama, R., Kageyama, M., Michel, E., & Paillard, D. (2009). Quantifying the roles

- of ocean circulation and biogeochemistry in governing ocean carbon-13 and atmospheric carbon dioxide at the Last Glacial Maximum. Climate of the Past, 5, 695–706.
 - Ullman, D., LeGrande, A., Carlson, A., Anslow, F., & Licciardi, J. (2014).
 Assessing the impact of Laurentide Ice Sheet topography on glacial climate.
 Climate of the Past, 10, 487–507.
- Völker, C., & Tagliabue, A. (2015). Modeling organic iron-binding ligands in a three-dimensional biogeochemical ocean model. *Marine Chemistry*, 173, 67–77.
- Waelbroeck, C., Paul, A., Kucera, M., Rosell-Melé, A., Weinelt, M., Schneider, R., Mix, A. C., Abelmann, A., Armand, L., Bard, E. et al. (2009). Constraints on the magnitude and patterns of ocean cooling at the Last Glacial Maximum.
 Nature Geoscience, 2, 127–132.
 - Weaver, A. J., Eby, M., Wiebe, E. C., Bitz, C. M., Duffy, P. B., Ewen, T. L., Fanning, A. F., Holland, M. M., MacFadyen, A., Matthews, H. D. et al. (2001). The UVic Earth System Climate Model: Model description, climatology, and applications to past, present and future climates. *Atmosphere-Ocean*, 39, 361–428.

690

- Winckler, G., Anderson, R. F., Jaccard, S. L., & Marcantonio, F. (2016). Ocean dynamics, not dust, have controlled equatorial Pacific productivity over the past 500,000 years. *Proceedings of the National Academy of Sciences*, 113, 6119–6124.
- Wunsch, C. (2016). Pore fluids and the LGM ocean salinity-Reconsidered. Quaternary Science Review, 135, 154–170.
- Zhao, N., Marchal, O., Keigwin, L., Amrhein, D., & Gebbie, G. (2018). A synthesis of deglacial deep-sea radiocarbon records and their (in) consistency with modern ocean ventilation. *Paleoceanography and Paleoclimatology*, .

Table 1: AMOC strength at 25° N (Sv) global/SO atmospheric iron fluxes (Tg Fe/y), and differences with PI_control in global dissolved inorganic carbon DIC (Pg C). For the iron fluxes, the numbers in parentheses indicate seasonal variability in the last significant digit. For the AMOC strengths, they indicate standard deviations in the last significant digit, taken from the last 500 y of the simulations.

| $\mathbf{Experiment}$ | AMOC | Atm. Fe flux | $\Delta { m DIC}$ |
|------------------------------|----------|-------------------|-------------------|
| PI_control | 17.79(2) | 0.053(5)/0.009(2) | - |
| LGM_13 | 13.51(1) | 0.096(7)/0.018(4) | -1153 |
| LGM_11 | 11.27(2) | 0.096(7)/0.018(4) | -936 |
| LGM_9 | 9.323(3) | 0.096(7)/0.018(4) | -805 |
| LGM_8 | 7.791(3) | 0.096(7)/0.018(4) | -738 |
| LGM_6 | 6.19(2) | 0.096(7)/0.018(4) | -706 |
| LGM_0 | 0.245(3) | 0.096(7)/0.018(4) | -791 |
| ${\rm LGM_13_SOFe}$ | 13.51(1) | 0.26(3)/0.18(4) | -656 |
| ${\rm LGM}_9_{\rm SOFe}$ | 9.323(3) | 0.26(3)/0.18(4) | -270 |
| ${\rm LGM}_{-}8_{\rm SOFe}$ | 7.791(3) | 0.26(3)/0.18(4) | -205 |
| ${\rm LGM_6_SOFe}$ | 6.19(2) | 0.26(3)/0.18(4) | -164 |

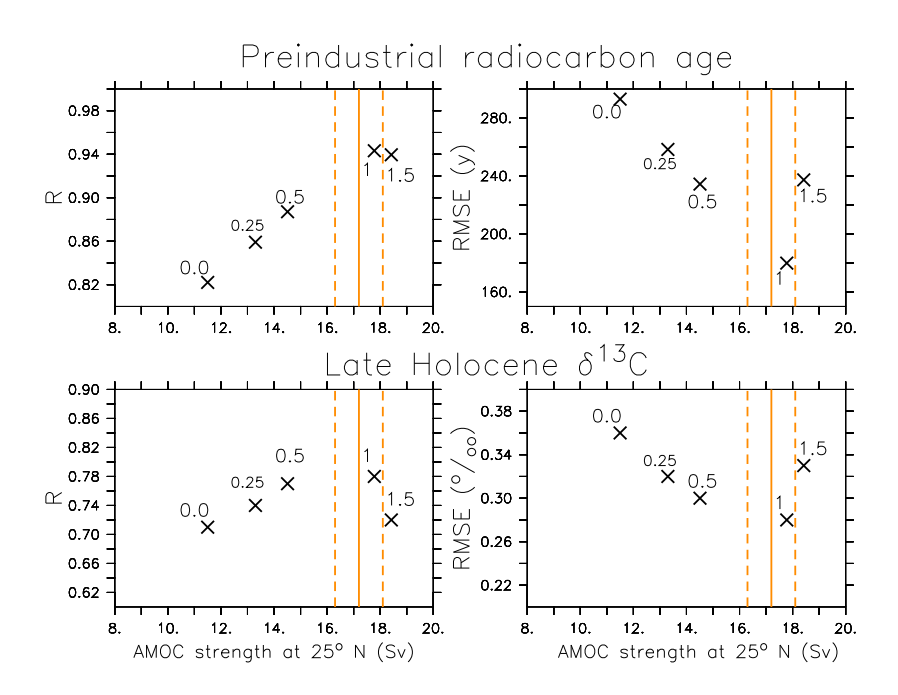


Figure 1: Comparison (R and RMSE) of different PI runs with measurements of water column natural radiocarbon ages (Key et al., 2004) and top-core sedimentary δ^{13} C from the late Holocene (Peterson et al., 2014). Each cross corresponds to a different simulation, generated by varying the meridional moisture diffusivity with a scale factor ϵ_q , indicated in the numbers next to each symbol. The simulations have AMOC strengths that range between 11.5 and 18.4 Sv. The orange full and dashed lines correspond to a modern estimate of AMOC strength at 26° N and its uncertainty (McCarthy et al., 2015).

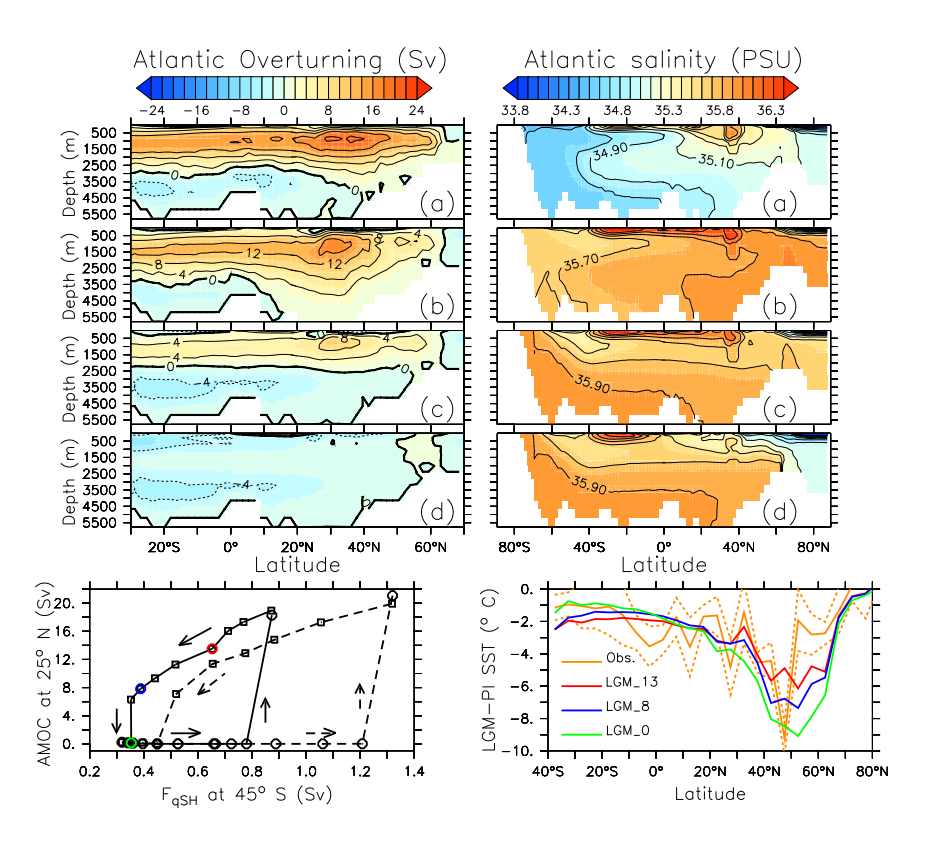


Figure 2: Top: Atlantic (left) meridional overturning and (right) zonally-averaged salinity for different simulated physical states; (a) PI_control, (b) LGM_13, (c) LGM_8, and (d) LGM_0. LGM salinities include a +1 addition due to lower sea level. Bottom left: Response of AMOC strength to (squares) decreases in southern hemisphere's meridional moisture transport (F_{qSH}) ; (circles) increases in F_{qSH} from a collapsed state. Full line curve uses PI + LGM anomalies for wind stress fields; dashed line curve uses PI wind stress fields. Bottom right: Atlantic zonally averaged LGM-PI sea surface temperature changes versus latitude for the same experiments, as indicated. Reconstructions (Waelbroeck et al., 2009) (full orange line) \pm propagated errors (dashed orange lines). Model means were calculated using only grid boxes from which there exist LGM reconstructions.

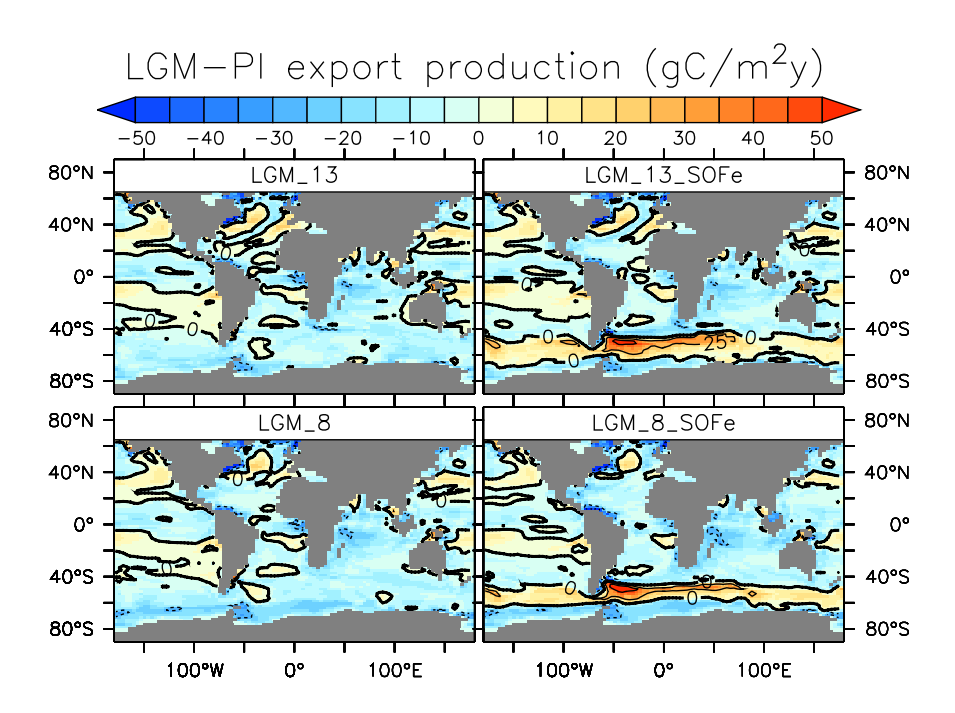


Figure 3: LGM-PI_control changes in export production out of the euphotic zone (80 m) for some of our simulations, as indicated.

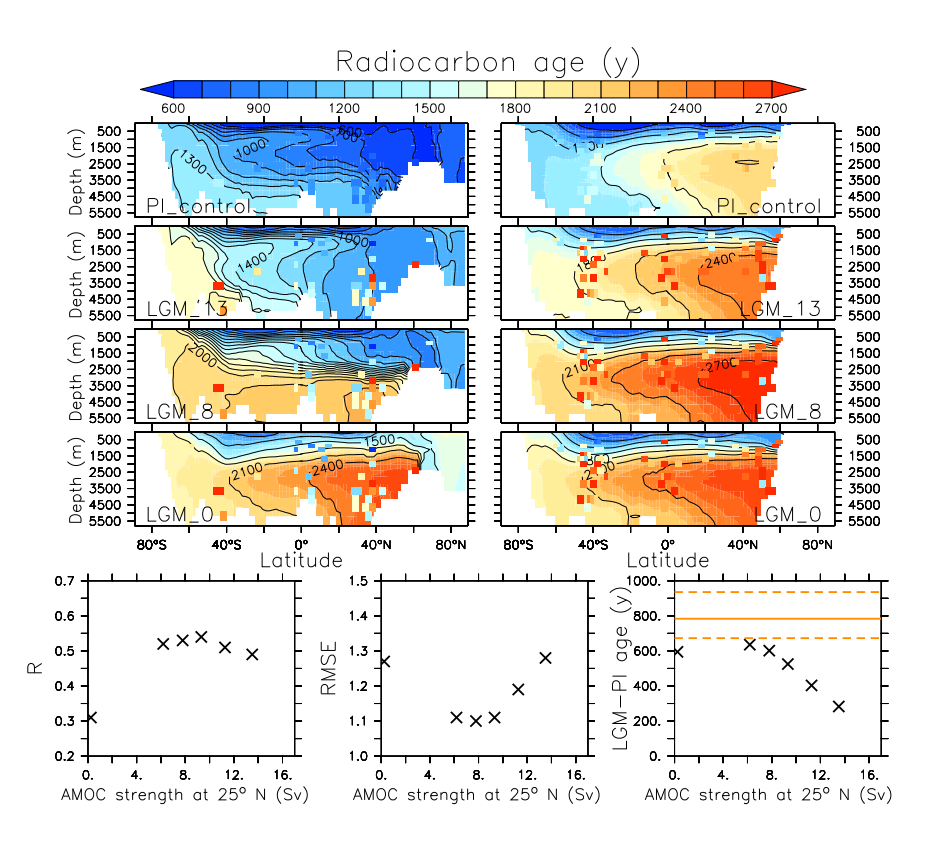


Figure 4: Top: Zonally averaged radiocarbon age sections from four representative experiments, as indicated. Left(right) corresponds to the Atlantic(Pacific) Ocean. Overlaid on the plots are data from the Global Data Analysis Project (Key et al., 2004) for PI_control and from a combination of sediment data (Skinner et al., 2017) for the rest. Bottom: Correlation coefficient R, uncertainty-normalized root mean square error (RMSE) and global LGM-PI relative age difference for all of our LGM experiments compared to reconstructions, as functions of AMOC strength. The orange line indicates the LGM-PI age difference from sediment reconstructions. The upper dashed line corresponds to the mean LGM-PI radiocarbon age difference if we include all data from Skinner et al. (2017) (see SM). The lower dashed line is calculated using our modeled LGM surface reservoir ages. The uncertainty used to normalize the RMSE is a combination of the data (620 14 Cyr, Skinner et al., 2017) and model (180 14 Cyr) uncertainties.

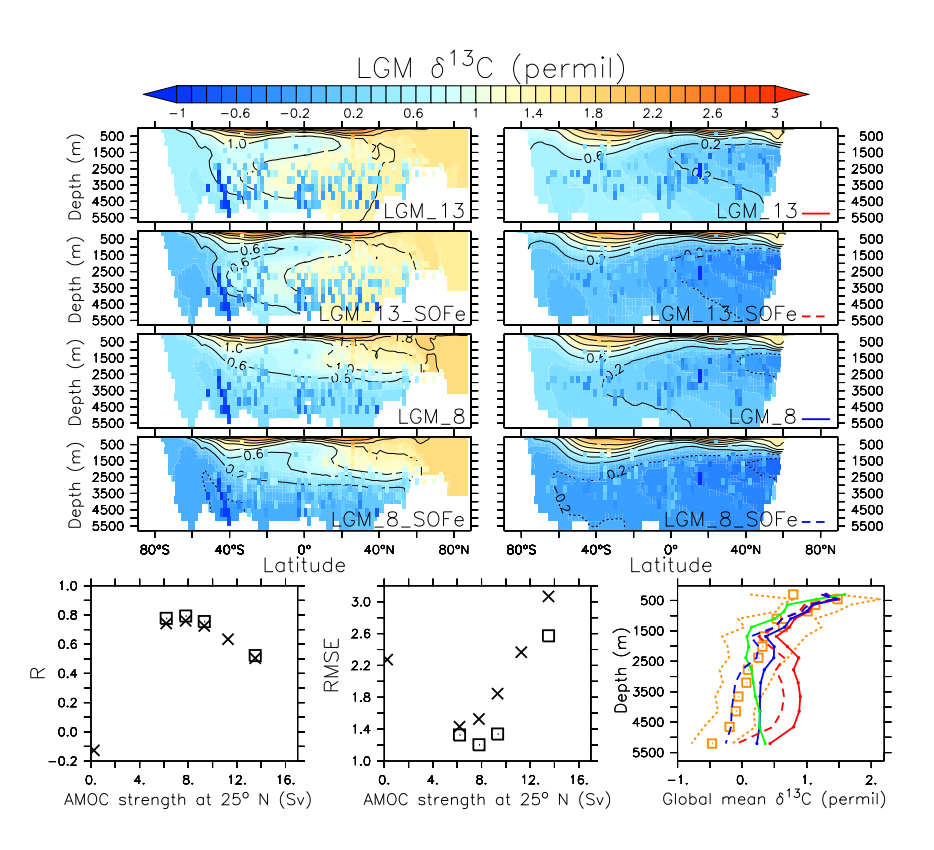


Figure 5: Top: Zonally averaged δ^{13} C sections from four of our LGM experiments, as indicated. Left (right) corresponds to the Atlantic (Pacific) Ocean. Overlaid on the plots are zonally-averaged LGM data from foraminifera (see SM). Bottom left and center: R and uncertainty-normalized RMSE from experiments compared to observations versus AMOC strength. Squares(crosses) represent simulations with(without) increased atmospheric soluble iron flux in the SO. The uncertainty used to normalize the RMSE is the standard deviation of PI_control δ^{13} C to top-core data (Schmittner et al., 2017) at the locations of LGM data, and equals 0.28 %. Bottom right: Depth profiles of global mean δ^{13} C, calculated using only grid boxes for which there exists LGM data. Red and blue: Experiments plotted in the meridional sections above, with line codes as indicated in the Pacific plots; green: LGM_0; Orange squares: Observations' global mean (squares) \pm standard deviations (dotted lines).

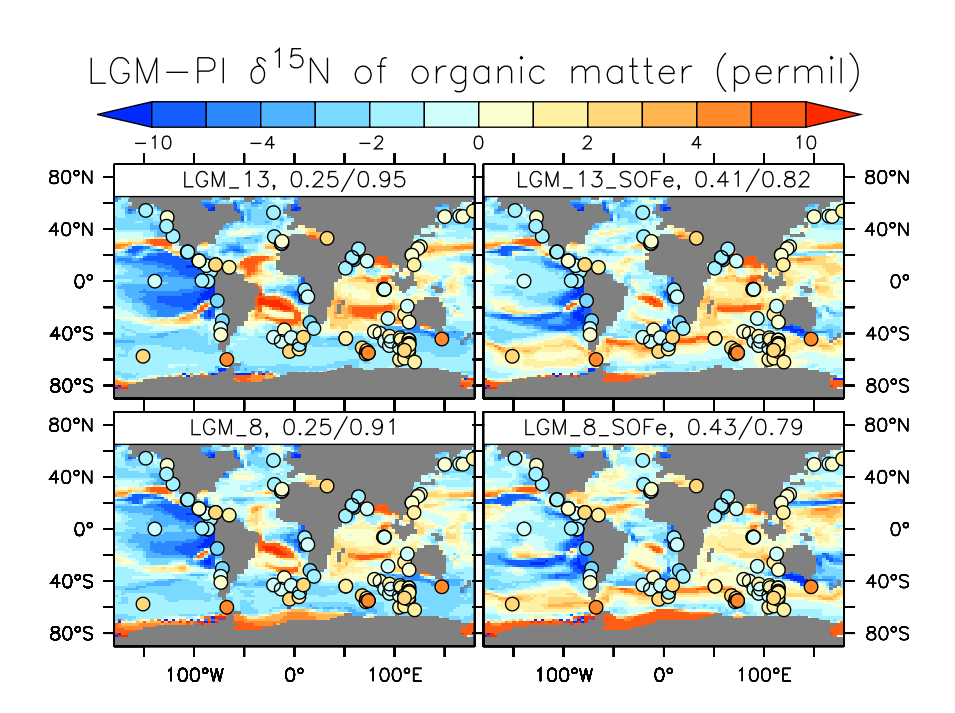


Figure 6: LGM-PI changes in $\delta^{15} N$ of detrital (particulate organic) matter, averaged over the top 120 m of the water column. Labels above each map indicate the experiment names, and also include the R/RMSE' of the simulations compared to observations, where RMSE' is the uncertainty-normalized RMSE of anomalies from the mean. Overlaid on the plots are LGM-PI values from observations (see SM).

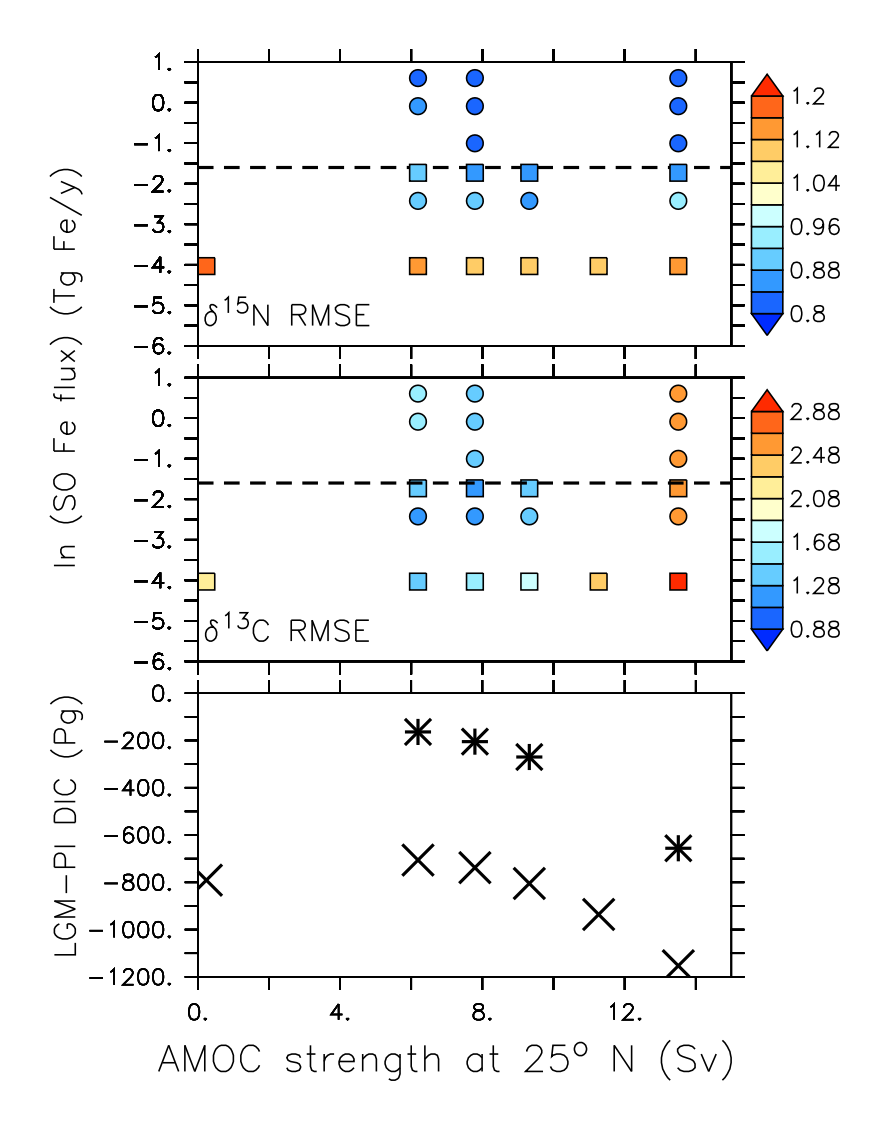


Figure 7: Uncertainty-normalized RMSE of modeled $\delta^{15}N$ and $\delta^{13}C$ compared to reconstructions, mapped over AMOC strength - logarithm of SO atmospheric soluble iron flux spaces. Squares correspond to the experiments described in the Experiments section. Circles are additional simulations performed with various increasing SO atmospheric soluble iron fluxes. The dashed line is an upper boundary estimate of LGM surface soluble iron fertilization from ice core data (Conway et al., 2015). Bottom: LGM-PI global DIC versus AMOC strength from our described LGM simulations. Stars (crosses) represent simulations with (without) increased atmospheric soluble iron flux in the SO.

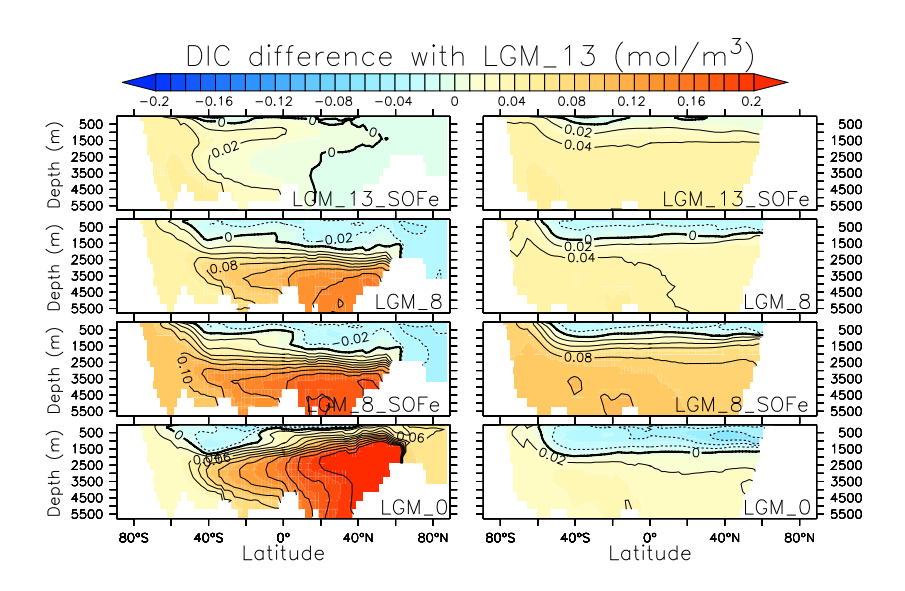


Figure 8: Differences in zonally-averaged DIC between some of our LGM simulations, as indicated, and LGM_13 , for the (left) Atlantic, and (right) Indo-Pacific oceans.